Title

Understanding the Adiabatic Evolution of Surface States in Tetradymite Topological Insulators under Electrochemical Conditions

Journal

The Journal of Physical Chemistry Letters, 15(10)

ISSN

1948-7185

Authors

Weng, Guorong
Laderer, William
Alexandrova, Anastassia N

Publication Date

2024-03-14

DOI

10.1021/acs.jpclett.4c00064

Understanding the Adiabatic Evolution of Surface States in Tetradymite Topological Insulators under Electrochemical Conditions

Guorong Weng,[†] William Laderer,[†] and Anastassia N. Alexandrova[*,†,‡]

[†]*Department of Chemistry and Biochemistry, University of California Los Angeles, Los Angeles, California, 90095, United States*

[‡]*Center for Quantum Science and Engineering, University of California Los Angeles, California, 90095, United States*

E-mail: ana@chem.ucla.edu

Abstract

Nontrivial surface states in topological materials have emerged as exciting targets for surface chemistry research. In particular, topological insulators have been utilized as electrodes in electrocatalytic reactions. Herein, we investigate the robustness of topological surface states and band topology under electrochemical conditions, specifically in the presence of an electric double layer. First-principles band structure calculations are performed on the electrified (111) surfaces of Bi_2Te_3, Bi_2Se_3, and Sb_2Te_3 using an implicit electrolyte model. Our results demonstrate the adiabatic evolution of the surface states upon surface charging. Under oxidizing potentials, the surface states are shifted upward in energy, preserving the Dirac point on the surface and the band inversion in the bulk. Conversely, under reducing potentials, hybridization is observed between the surface and bulk states, suggesting a likely breakdown of topological protection. The position of the Fermi level, which dictates the working states in catalytic reactions, should ideally be confined within the bulk bandgap. This requirement defines a potential window for the effective application of topological electrocatalysis.

TOC Graphic

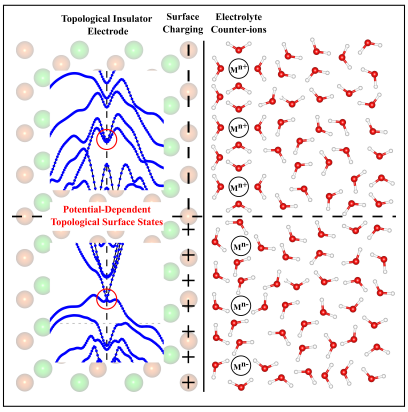

Keywords

topological surface states, topological insulators, electrocatalysis, surface charging, electric double layer

Topological materials (TMs) are increasingly recognized as a new generation of catalysts, with the potential to replace precious metals in heterogeneous catalysis.[1–5] The conducting electronic states in TMs, known as topological surface states (TSSs), are protected by the specific symmetries of bulk crystals and show promise in enhancing catalytic activity, durability, and efficiency. To date, topological insulators,[6–14] crystalline insulators,[15–17] and semimetals[18–38] have been explored in various catalytic applications, with notable enhancements reported. However, the exact role of TSSs in catalysis remains elusive, primarily due to the challenges of in situ measurements under complex reaction conditions. As a result, theoretical simulations have become crucial for understanding the contributions of TSSs in catalysis.

Topological insulators (TIs) containing heavy elements exhibit band inversion in their bulk band structures due to strong spin-orbit coupling (SOC), leading to an insulating bandgap in the bulk while sustaining otherwise gapless surface states. The tretradymite family–Bi_2Se_3, Bi_2Te_3, and Sb_2Te_3–is recognized as three-dimensional TIs, characterized by a single Dirac point on their surface.[39–48] Their simple and straightforward TSSs have made them prototypical materials for exploring the role of TSSs in practical applications such as electrocatalysis. Recent studies have highlighted the stability of their TSSs in the presence of adsorbates, defects, and surface oxidation.[14,49–53] However, there is a significant gap between the systems in actual electrochemical environments and those evaluated in experimental or theoretical characterizations.[5] Particularly, under electrocatalytic conditions, an electric double layer (EDL) forms at the solid-liquid interface where the electrolyte ions balance the charges on the electrode surface. As a key feature in electrocatalysis, the EDL remarkably affects the local reaction environment,[54–56] yet its effect on TSSs has not been thoroughly explored. Therefore, it is critical to consider surface charging and electrolyte ions in theoretical calculations to understand the interplay of EDL with TSSs.

Density functional theory[57,58] (DFT) methods, employing the generalized gradient approximation[59] and SOC, have been widely used to access topological band structures, align-

ing well with angle-resolved photoemission spectroscopy (ARPES) results.[40,42,46,60] Additionally, the complex solid-liquid interface can be effectively approximated by a cost-effective implicit electrolyte model based on the linearized Poisson-Boltzmann equation.[61,62] In practice, plane-wave DFT calculations within the Vienna Ab initio Simulation Package (VASP)[63–66] and the VASPsol[67,68] implementation offer a robust approach for describing surface dynamics in the presence of an electric double layer.[69–72]

In this work, we focus on elucidating the electrostatic effects of EDL on the TSSs of the tetradymite TIs family through first-principles calculations. The electrodes are modeled as two-dimensional slabs immersed in an implicit electrolyte solution, with surface charging achieved by varying the number of electrons in the systems and solving linearized Poisson-Boltzmann equation.[61,62] All calculations are performed using the VASP[63–66] package along with the VASPsol implementation.[67,68] This study does not consider the presence of surface adsorbates and defects, nor does it account for the chemical changes resulting from surface oxidation or reduction that may occur under applied potentials. We investigate the properties of charged slabs in an equilibrium state, thus computing their ground-state electronic band structures. The presence of the EDL significantly alters the surface Dirac point and the Fermi level within the band structures. The surface states exhibit distinct behaviors as the applied potential sweeps from negative to positive. Under oxidizing (positive) potentials, the surface states shift upward in energy, enlarging the energy gap between the Dirac point and the bulk bands. As a result, the band inversion is preserved, and the robustness of the TSSs persists. However, when reducing potentials are applied, the surface states shift downward, crossing the bulk bands and leading to hybridization of the surface and bulk states. Consequently, the original surface states extend into the bulk, implying a likely breakdown of topological protection. The Fermi level also exhibits a dependence on the applied potential. To avoid intersection of the Fermi level with the bulk bands, a potential window is proposed to define a reasonable range for surface charging. We argue that this window is critical for considerations of topological electrocatalysis and for leveraging the

advantages of TSSs in the tetradymite TIs.

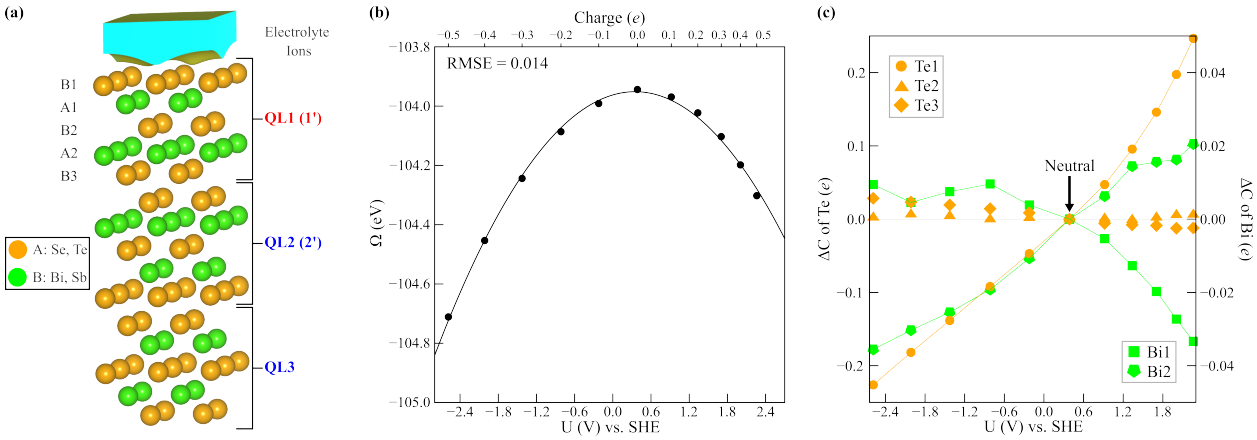

Figure 1: (a) Slab model used in surface charging DFT calculations for the three tetradymite topological insulators. The isosurface above the B1 atomic layer represents the counter-charge density generated by VASPsol. Owing to the inversion symmetry, only three of the five quintuple layers are shown here, and they are labelled for further analysis. (b) Grand canonical energy (Ω) of the Bi_2Te_3 slab plotted as a function of the electrode potential relative to the standard hydrogen electrode potential. The plotted data points are fitted to a parabolic curve, with a root-mean-square error of 0.014. (c) Bader charge analysis on the individual ions within QL1 (1') of the Bi_2Te_3 slab. The values of ΔC are calculated with respect to the charge-neutral slab, with the left vertical axis assigned for the Te ions and the right one for the Bi ions. The solids lines guide the reading for the three ions of interest.

Figure 1a presents the slab model used for surface charging calculations of the three tetradymite TIs: Bi_2Se_3, Bi_2Te_3, and Sb_2Te_3. The bulk crystal of these compounds exhibits a layered structure, where a quintuple layer (QL) is defined by five atomic layers of the A_2B_3 stoichiometry. Neighboring QLs are bound by weak Van der Waals interactions, making it a convenient choice (due to low surface energy and preservation of charge neutrality and stoichiometry) to cut through the inter-QL gap for the (111) surface. Five quintuple layers from the relaxed bulk crystal are extracted to form the slab, where QL1 and 1' refer to the two surface QLs, QL2 and 2' to the two subsurface QLs, and QL3 to the central layer of the slab. Owing to inversion symmetry, the two slab surfaces are identical, and only one side is shown in Figure 1a. Positioned above the slab surface is the counter-charge density isosurface, representing the implicit electrolyte ions. The electric field created by these ions is solved self-consistently to balance the surface charges. All computational results are detailed

in the Supporting Information, which we reference in our discussion. In the following text, we primarily discuss the results exemplified by Bi_2Te_3 and draw comparisons with Bi_2Se_3 and Sb_2Te_3.

The Bi_2Te_3 slab is charged by altering the number of electrons of the system in the calculations, ranging from -0.5 e to $+0.5$ e relative to the charge-neutral slab. This effectively means that the charged slab represents a grand canonical ensemble of electronic states, where the number of electrons varies in response to the applied (chemical) potential. The surface QLs are fully relaxed for each charging state, showing negligible differences from the zero-charging state. The Fermi energy, obtained from the negatively and positively charged slabs, translates into the electro-reduction and electro-oxidation potentials (U), respectively, via Eq.S1. Figure1b illustrates the potential window under investigation, sweeping from -2.6 V (reduction) to 2.4 V (oxidation) versus the standard hydrogen electrode (SHE). The corresponding charges to the applied potentials are indicated on the upper horizontal axis. Moreover, the grand-canonical free energy (Ω) is plotted as a function of U and is further fitted to a parabolic curve. The low root-mean-square error (RMSE) of this fitting suggests that, within the potential window under consideration, the EDL formed at the solid-liquid interface behaves as an ideal capacitor.[73] A similar behavior is observed for the slabs of Bi_2Se_3 and Sb_2Te_3, as shown in Figure S3.

To understand the distribution of charges under an applied potential, Bader charge analysis[74–76] is performed on each individual atom (see Tables S8-S16). First, we analyze the charge-neutral slab. Owing to the difference in electronegativity between Bi and Te, the Te atoms gain electrons and form "anions," while the Bi atoms form "cations" by losing electrons. For the surface QLs, the Bader charges for Te are found to be -0.47 e, -0.66 e, and -0.45 e for Te1, Te2, and Te3, respectively. In contrast, the Bader charges for Bi are predicted to be $+0.80$ e (Bi1) and $+0.78$ e (Bi2), resulting in a zero net charge within QL1 (1').

When an electrode potential is applied, we calculate the differential Bader charge (ΔC)

to track the evolution of the charging state for each ion. First, we focus on the ions within QL1 (1') of the Bi_2Te_3 slab. The results are summarized in Figure 1c, where the left vertical axis is assigned for Te and the right one for Bi. For the oxidized surface with a positive U, over 80% of the changes in the total charge are found on the Te1 layer (orange line and circles), while the Bi2 ions (green line and pentagons) show only slight oxidation. Counter-intuitively, the Bi1 ions (green line and squares) are predicted to undergo reduction when $U > 0$. Similarly, when a negative U is applied, more than 80% of the negative charges localize on the Te1 ions, with the Bi2 cations experiencing minimal reduction.

For QL2 (2'), the most noticeable changes in charging states primarily occur in the Te1 and Bi1 ions (see Figure S4), owing to their proximity to the surface QLs. The other ions within QL2 (2') and those in QL3 show minimal impact, with $|\Delta C| \leq 0.01\ e$ in all cases (as detailed in Tables S12 and S13). It is noteworthy that the surface charging of the Sb_2Te_3 slab behaves similarly to that of Bi_2Te_3 (as indicated in Figure S4). However, when Te is replaced by Se, the behavior of the Bi1 ions consistently aligns with that of the Se1 ions at negative U, contrasting with the trend of Bi1 in Figure 1c. This discrepancy can be ascribed to the increased electronegativity of Se compared to Te, thereby enhancing the ionic character of Bi_2Se_3, in which the Bi ions are more electron-deficient than in Bi_2Te_3.

In the following analysis, we examine the effect of surface charging on the band structures of the Bi_2Te_3 slab under various applied potentials. Specifically, our focus is on the surface Dirac point and the bulk state that exhibits the band inversion.

Figure 2 presents four representative charging states ($\pm 0.2\ e$ and $\pm 0.4\ e$) in comparison with the charge-neutral slab. In the upper panels, the band structures are spatially resolved by projecting the electronic states onto the surface QLs and the bulk QLs. By evaluating the trace of the projected particle density of all spinor states, the surface-predominant states are depicted in red while the bulk states are denoted in blue. The corresponding applied potentials and charges are indicated at the top. The distinct color-labelling for the surface states tracks the evolution of the surface Dirac point (highlighted as insets in the upper panels

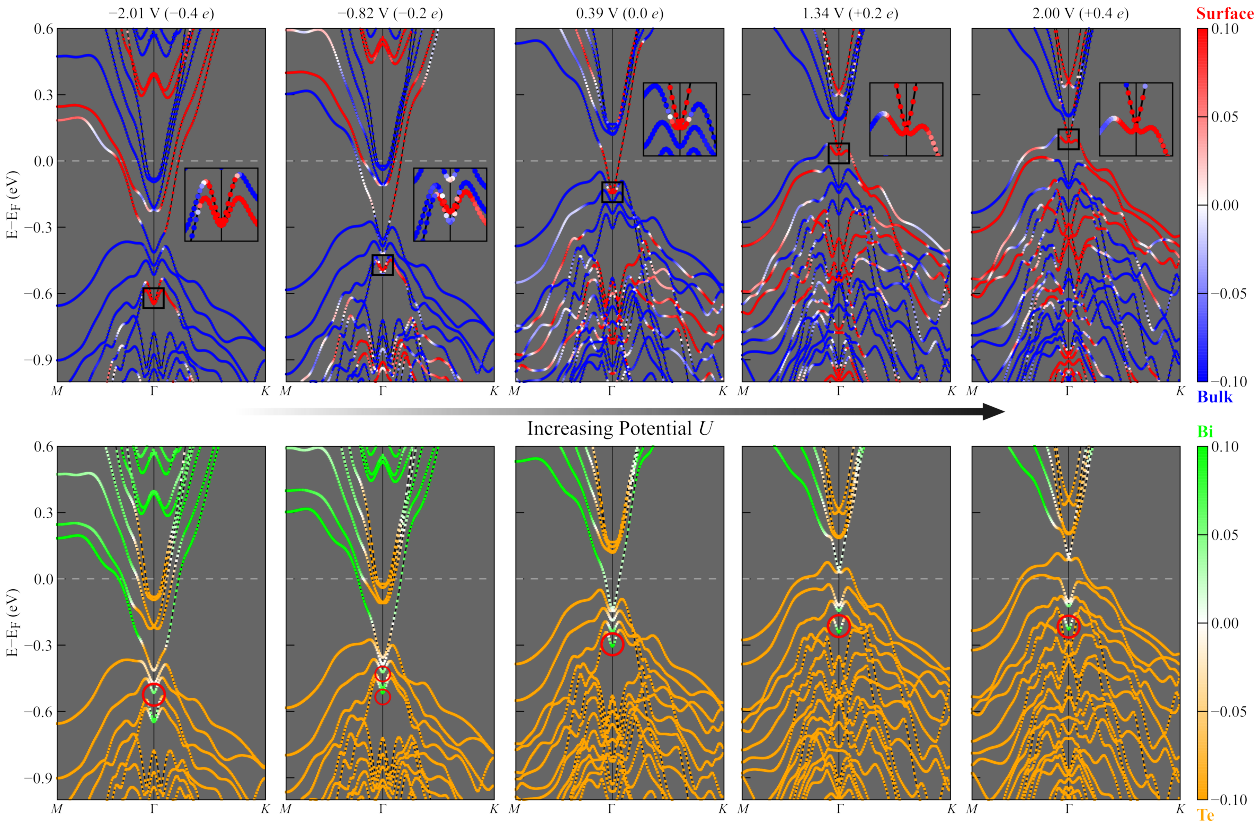

Figure 2: Projected band structures of the Bi_2Te_3 slab under various electrode potentials. In each panel, the electronic states are color-coded to reflect their predominant orbital contributions. Upper panels: electronic states depicted in red are primarily derived from the surface, while those in blue are dominated by the bulk. Lower panels: electronic states depicted in green originate primarily from the Bi atoms, while those in orange are Te-dominated. The black squares in the upper panels track the evolution of the surface Dirac point, which is further highlighted in the inset. The red circles in the lower panels highlight the electronic states that exhibit band inversion around the Γ point.

of Figure 2) in response to the electrode potential in the adiabatic limit. The full set of band structures for all charging states are listed in Figures S7-S11. Under positive potentials, the Fermi level shifts downward below the Dirac point, corresponding to an electron-accepting state for oxidation reactions. The energy gap between the Dirac point and the bulk valence bands increases as U gets more positive. In addition to the Dirac point, other surface-predominant states are generally shifted up and toward the Fermi level, as shown by the population of the red states (see the top right panels in Figure 2) along the two investigated k-paths. Under negative potentials, the Fermi level shifts up in energy, populating both the surface (red) and bulk (blue) states in the (original) conduction band. Compared with the bulk valence bands, the Dirac point is significantly stabilized in energy, drilling down away from the Fermi level and crossing the bulk valence bands. With $U < -1.43$ V, the Dirac-point states are robust, i.e., they remain localized on the surface QLs (see Figure S7). However, these surface states can hybridize with the bulk states (which are analyzed in the following) when a less negative reducing potential is applied (see $U = -0.82$ V in Figure 2 and $U = -0.22$ V in Figure S7).

In the lower panels of Figure 2, we project the electronic states of the Bi_2Te_3 slab onto Bi and Te to evaluate the predominant elemental character. Electronic states originating primarily from Bi are depicted in green, while Te-dominated states are shown in orange. In conjunction with the upper panels, the electronic states denoted simultaneously in blue and green represent Bi-predominant states in the bulk. At the Brillouin zone center (Γ), the "green" state resembles the one exhibiting band inversion in the bulk crystal, as evidenced by their shared Bi-p_z orbital components (see Figures S5 and S10). These states do not appear inverted to the valence band when SOC is disabled in the calculations for the slab in vacuum (Figure S6). Thus, the band inversion phenomenon can be attributed to this Bi-p_z state, which is localized in the bulk QLs of the slab.

When an oxidizing potential is applied, the band inversion remains largely unaffected, while the surface Dirac point shifts upwards, increasing the gap from the inverted occupied

states in the bulk (see the bottom right panels in Figure 2). As a result, the surface states are consistently protected by the robust band topology. In contrast, under reducing potentials, the surface states move in the opposite direction. For U at -0.22 V (Figure S10) and -0.82 V (lower panels in Figure 2), the inverted state splits into two bands due to hybridization with the Dirac-point states. Driven by energy degeneracy, the hybridized states exhibit primarily Bi-p_z orbital character. As the reducing potential becomes more negative ($U < -1.43$ V, see Figure S10), the Dirac-point states surpass the entire frontier bulk bands, eliminating the hybridization and splitting. Consequently, both the Dirac point and the band inversion are restored, as shown in Figure 2 at $U = -2.01$ V. It is worth noting that the a similar evolution of TSSs with significant state hybridization is observed at negative U in a 7-QL Bi_2Te_3 slab (see Figure S9), suggesting that this phenomenona is consistent regardless of the slab thickness.

The electronic band structures of the Bi_2Se_3 and Sb_2Te_3 slabs exhibit a similar evolution in response to the applied potential: under positive U, both the Dirac point and band inversion remain robust against surface charging; however, the surface states can hybridize with the inverted Bi/Sb-p_z states under certain negative potentials. Moreover, the response of the surface states to surface charging is more pronounced than that of the bulk states, exhibiting energy stabilization at negative U and destabilization at positive U. These effects are clearly illustrated by the projected density of states (see Figures S20-S22).

The distinct behavior of the surface states, including the Dirac point, should be attributed to the combined effects of surface charging and the presence of electrolyte ions, which are the two major components of the EDL. As the implicit electrolyte model only provides an electric field at the interface, our discussion is confined to the electrostatic interactions between the surface and the electrolyte ions. First, we analyze the electron density fluctuations upon surface charging. Figure 3a displays the one-dimensional electron density as a function of position along the z-axis for three representative charging states (0 and $\pm 0.5\, e$). The electron density is integrated over the xy-plane at each sampled z position, with the grey dotted lines

indicating the atomic positions within QL1 (1'). The magenta bar marks the z position at which the integrated counter-charge density reaches a maximum (see Figure S23), signifying the concentrated accumulation of electrolyte ions. Under negative charging ($U < 0$, blue line and circles), there is an increase in electron density at the interface compared to the charge-neutral slab (black line and squares), corresponding to surface charging and the reduction of Te1. In the Bi1-Te2 and Bi2-Te3 regions, the electron density is also observed to be higher than that of the zero-charging case. However, in regions like Te1-Bi1 and Te2-Bi2, the electron density decreases, indicating oxidizing behavior under reducing potentials. For positive charging (red line and diamonds), the variation in integrated density is symmetric to the negative-charging one, differing only by a sign and reverting the electron-gaining and -losing regions.

The coexistence of reduced and oxidized species is consistent with the differential Bader charge analysis shown in Figure 1c, indicating the formation of induced dipoles within QL1 (1') relative to the charge-neutral slab. We calculate the electron density difference in a three-dimensional real-space grid, and the results for QL1 (1') are presented in Figure 3b. The alternating yellow and blue colors represent the induced dipoles, which are further labelled by circles marked with "+" and "-" charges. In the bulk QLs, the formation of induced dipoles is not observed, as the integrated electron density remains largely unaffected by surface charging (see Figures S24). The absence of induced dipoles in the bulk QLs can be attributed to the weakened interactions across the gap between two adjacent QLs and the fact that the bulk is insulating.

Compared with the charge-neutral slab in vacuum, the electrostatic effects induced by surface charging originate from two sources: (1) the accumulation of electrolyte ions at the interface, and (2) the induced dipoles confined within the surface QLs. The former is included in the ionic (external) potential term V_{ion}, while the latter is represented by the Hartree term V_{H} in the single-particle Hamiltonian. The plane-averaged total electrostatic (ES) potential, $V_{ion} + V_{\mathrm{H}}$, is plotted as a function of position in Figure 3c for the three charging states. For

comparison, the curves are aligned to the minimum potential of QL3, as the bulk properties are considered invariant. In the charging state with -0.5 e, the total ES effects exhibit stabilization at all atomic positions, where the blue curve is energetically lower than the black one. In inter-atomic regions, such as Te1-Bi1 and Te2-Bi2, the ES effects are observed to be opposite. However, for surface electronic states localized around the ions (atoms), the onsite interactions are much stronger. As a result, the stabilization effects stemming from the electrolyte cations dominate the energy shifts for the surface states, explaining the downward movement of the Dirac point at negative U, as shown in Figure 2. Furthermore, the induced surface dipoles effectively screen the electrostatic interactions between the electrolyte ions and the bulk QLs, rendering much weaker effects on the bulk electronic states. A similar analysis applies to the $+0.5$ e charging state, where we observe destabilization of the ES effects due to the electrolyte anions. Consequently, the surface states, including the Dirac point, are shifted upward in energy at positive U (Figure 2). The evolution of TSSs under such counter-ion-dominated electrostatic effects is comparable to the tuning of the topological band structures by an external electric field.[77–82]

The ES effects on the surface states, as discussed above, are observed to be the same for the Bi_2Se_3 and Sb_2Te_3 slabs (see Figures S25-S26), corroborating their similar evolution of band structures under applied potentials. It is important to note that under surface charging conditions, both the Fermi level and the surface electronic states dynamically evolve. For topological catalysis considerations, the working states should strictly be those surface states that are protected by band topology. This necessitates that the Fermi level be located within the bulk bandgap and not cross the bulk bands. For example, in Figure 2, the Fermi level intersects both the surface and bulk conduction bands at $U = -2.01$ V and $U = -0.82$ V. Under these conditions, both the surface and the bulk are conducting, and the catalytic mechanism is likely reduced to classical catalysis where topology plays no significant role. However, this bulk-crossing issue is more manageable under positive potentials due to the separation of the surface states from the bulk. For electrocatalytic oxidation reactions on

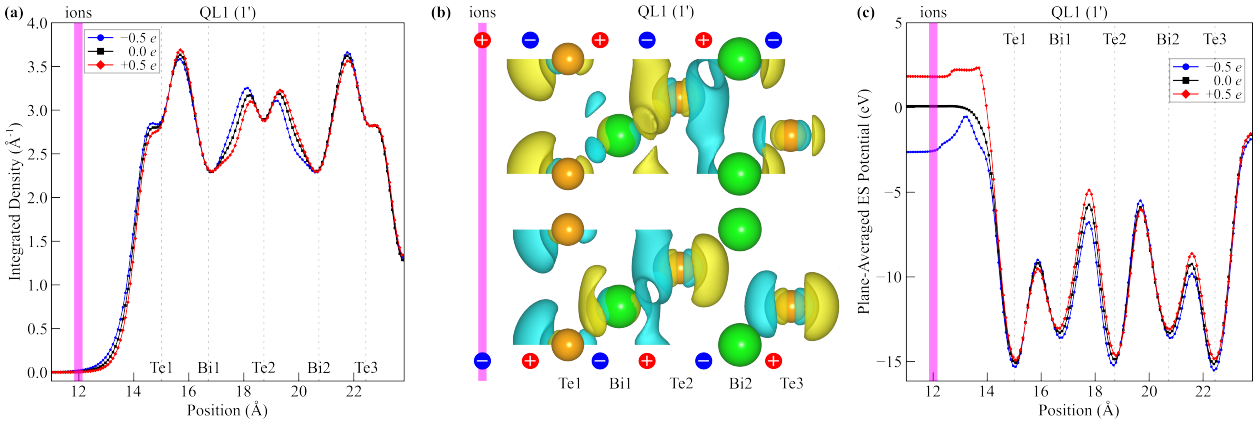

Figure 3: (a) Integrated electron density over the xy-plane at various sampled positions along the z-axis (perpendicular to the surface) of the Bi_2Te_3 slab. The plot focuses on QL1 (1') where apparent electron density fluctuations occur in response to surface charging (black for 0 e, red and blue for $+0.5$ e and -0.5 e, respectively). The grey dotted lines denote the ionic positions, and the magenta bar marks the peak of the integrated counter-charge density, which is ~ 3 Å away from the surface. (b) Visualization of the change in electron density in a three-dimensional real space grid. Relative to the charge-neutral slab, regions gaining electrons are shown in yellow, while regions losing electron are in cyan. Induced dipoles are inferred from these density fluctuations and indicated by blue and red circles. (c) Plane-averaged electrostatic (ES) potential within QL1 (1') along the z-axis for the same three charging states in (a).

the (111) surface of Bi_2Te_3, the applied potential can be raised to 1.34 V while preserving the TSSs. To define the potential range that avoids bulk-crossing, we calculate the band structures within a narrower range of surface charging (Figures S27-S32). The determined potential windows (in unit V vs. SHE) are $[-0.10, 1.34]$ for Bi_2Te_3, $[0.72, 3.06]$ for Bi_2Se_3, and $[-0.46, 1.42]$ for Sb_2Te_3. These findings suggest that Bi_2Se_3 is ideal for catalyzing oxidation reactions, while Sb_2Te_3 is more suitable for reduction reactions.

In summary, we have detailed the profound effects of surface charging on the band structures of the three tetradymite TIs through first-principles calculations. We observed that the surface states undergo significant evolution under electrochemical conditions. When an oxidizing potential is applied, the surface states shift upwards in energy due to the destabilizing effects from the electrolyte anions, while the separation of the Dirac point from the bulk bands helps preserve the band inversion. Conversely, under reducing potentials, the Dirac-point states are stabilized by the electrolyte cations. This can lead to hybridization

with the inverted Bi/Sb-p_z states when they intersect with the bulk bands, potentially indicating the loss of topological protection. It is important to acknowledge that the surfaces of TIs can undergo significant reconstructions under applied potentials, particularly at very negative and very positive potentials. Such reconstructions could influence the evolution of the surface states, potentially by changing the surface stoichiometry. A detailed investigation into the surface reconstruction effects on TSSs is planned for future research.

Besides the evolution of TSSs, accurately locating the Fermi level is also crucial, as it determines the electronic states responsible for donating or accepting electrons in chemical reactions. In topological catalysis involving TIs, the Fermi level should ideally be confined within the bulk bandgap. This confinement necessitates a reasonable range for applied potentials. The potential windows identified in our study suggest that Bi_2Se_3 is more suitable for electrocatalytic oxidation reactions, while Sb_2Te_3 is better suited for catalyzing reduction reactions.

Our findings underscore the importance of considering the evolution of TSSs and the position of the Fermi level under electrochemical conditions when using topological insulators in electrocatalysis. The rigid band model, lacking the dynamics of surface states, is inadequate to be a descriptor for effectively evaluating topological electrocatalysis. For future design of toplogical catalysts, it is crucial to achieve a high density of TSSs and ensure well-separated surface bands from the bulk bands, particularly for cathodic applications in electrocatalysis. We believe this work will provide valuable insights for simulating electrocatalysis with topological insulators, highlighting that the effects of surface charging deserve as much attention as the presence of defects and adsorbates.

Acknowledgement

The authors thank Dr. Harry W. T. Morgan for helpful discussion on the manuscript. This work was supported by the Brown Science Foundation Award 1168 to A. N. A. The com-

putations utilized the following resources (1) computational and storage services associated with the Hoffman2 Shared Cluster provided by UCLA Office of Advanced Research Computing's Research Technology Group, (2) Perlmutter of the National Energy Research Scientific Computing Center (NERSC), a U.S. Department of Energy Office of Science User Facility operated under Contract DE-AC02-05CH11231, and (3) Bridges-2 at the Pittsburgh Super Computing center supported by the ACCESS project No.CHE230055p.

Supporting Information Available

Text: computational details for the slabs and bulk crystals; Tables: input parameters used in VASP calculations, lattice vectors for the relaxed bulk crystals and slabs, numerical results from Bader charge analysis; Figures: slab models used in DFT calculations, bulk crystals used in band structure calculations, grand-canonical free energy plotted as a function of the applied potential, differential Bader charge analysis as a function of the applied potential, band structures of the bulk crystals and the identification of the inverted state in the bulk, band structures of the slabs in vacuum with and without SOC, projected band structures under various charging conditions, Dirac-point wavefunctions and the inverted state wavefunctions under various charging conditions, projected density of states under various charging conditions, one-dimensional counter-charge density as a function of the z position, one-dimensional electron density and plane-integrate electrostatic potential as a function of the z position.

References

(1) Li, G.; Felser, C. Heterogeneous Catalysis at the Surface of Topological Materials. *Appl. Phys. Lett.* **2020**, *116*, 070501.

(2) Xie, R.; Zhang, T.; Weng, H.; Chai, G.-L. Progress, Advantages, and Challenges of Topological Material Catalysts. *Small Sci.* **2022**, *2*, 2100106.

(3) Luo, H.; Yu, P.; Li, G.; Yan, K. Topological Quantum Materials for Energy Conversion and Storage. *Nat. Rev. Phys.* **2022**, *4*, 611–624.

(4) Zhang, X.; Wang, L.; Li, M.; Meng, W.; Liu, Y.; Dai, X.; Liu, G.; Gu, Y.; Liu, J.; Kou, L. Topological Surface State: Universal Catalytic Descriptor in Topological Catalysis. *Mater. Today* **2023**, *67*, 23–32.

(5) Yang, Q.; Zhang, Y.; Sun, Y.; Felser, C.; Li, G. Topological Catalysis in the Language of Chemistry. *Innov. Mater.* **2023**, *1*, 100013.

(6) Chen, H.; Zhu, W.; Xiao, D.; Zhang, Z. CO Oxidation Facilitated by Robust Surface States on Au-Covered Topological Insulators. *Phys. Rev. Lett.* **2011**, *107*, 056804.

(7) Chen, S.; Fang, Y.-M.; Li, J.; Sun, J.-J.; Chen, G.-N.; Yang, H.-H. Study on the Electrochemical Catalytic Properties of the Topological Insulator Bi_2Se_3. *Biosens. Bioelectron.* **2013**, *46*, 171–174.

(8) He, Q. L.; Lai, Y. H.; Lu, Y.; Law, K. T.; Sou, I. K. Surface Reactivity Enhancement on a Pd/Bi_2Te_3 Heterostructure through Robust Topological Surface States. *Sci. Rep.* **2013**, *3*, 2497.

(9) Xiao, J.; Kou, L.; Yam, C.-Y.; Frauenheim, T.; Yan, B. Toward Rational Design of Catalysts Supported on a Topological Insulator Substrate. *ACS Catal.* **2015**, *5*, 7063–7067.

(10) Li, L.; Zeng, J.; Qin, W.; Cui, P.; Zhang, Z. Tuning the Hydrogen Activation Reactivity on Topological Insulator Heterostructures. *Nano Energy* **2019**, *58*, 40–46.

(11) Qu, Q.; Liu, B.; Liang, J.; Li, H.; Wang, J.; Pan, D.; Sou, I. K. Expediting Hydrogen

Evolution through Topological Surface States on Bi_2Te_3. *ACS Catal.* **2020**, *10*, 2656–2666.

(12) Li, G.; Huang, J.; Yang, Q.; Zhang, L.; Mu, Q.; Sun, Y.; Parkin, S.; Chang, K.; Felser, C. MoS_2 on Topological Insulator Bi_2Te_3 Thin Films: Activation of the Basal Plane for Hydrogen Reduction. *J. Energy Chem.* **2021**, *62*, 516–522.

(13) Wei, Y.-H.; Ma, D.-S.; Yuan, H.-K.; Wang, X.; Kuang, M.-Q. Topological Insulator Path Toward Efficient Hydrogen Evolution Catalysts in the Li_2Pt family. *Phys. Rev. B* **2023**, *107*, 235414.

(14) Li, J.; Wu, J.; Park, S.-w.; Sasase, M.; Ye, T.-N.; Lu, Y.; Miyazaki, M.; Yokoyama, T.; Tada, T.; Kitano, M. et al. Topological Insulator as an Efficient Catalyst for Oxidative Carbonylation of Amines. *Sci. Adv.* **2023**, *9*, eadh9104.

(15) Xie, H.; Zhang, T.; Xie, R.; Hou, Z.; Ji, X.; Pang, Y.; Chen, S.; Titirici, M.-M.; Weng, H.; Chai, G. Facet Engineering to Regulate Surface States of Topological Crystalline Insulator Bismuth Rhombic Dodecahedrons for Highly Energy Efficient Electrochemical CO_2 Reduction. *Adv. Mater.* **2021**, *33*, 2008373.

(16) Qu, Q.; Liu, B.; Liu, H.; Liang, J.; Wang, J.; Pan, D.; Sou, I. K. Role of Topological Surface States and Mirror Symmetry in Topological Crystalline Insulator SnTe as an Efficient Electrocatalyst. *Nanoscale* **2021**, *13*, 18160–18172.

(17) Jiang, Z.; Zhang, T.; Rappe, A. M. Topological Bismuth $(1\bar{1}0)$ Facet for Efficient Oxygen Reduction Cathode in Fuel Cells. *J. Phys. Chem. C* **2023**, *127*, 19879–19885.

(18) Rajamathi, C. R.; Gupta, U.; Kumar, N.; Yang, H.; Sun, Y.; Süß, V.; Shekhar, C.; Schmidt, M.; Blumtritt, H.; Werner, P. et al. Weyl Semimetals as Hydrogen Evolution Catalysts. *Adv. Mater.* **2017**, *29*, 1606202.

(19) Li, G.; Sun, Y.; Rao, J.; Wu, J.; Kumar, A.; Xu, Q. N.; Fu, C.; Liu, E.; Blake, G. R.; Werner, P. et al. Carbon-Tailored Semimetal MoP as an Efficient Hydrogen Evolution Electrocatalyst in Both Alkaline and Acid Media. *Adv. Energy Mater.* **2018**, *8*, 1801258.

(20) Li, J.; Ma, H.; Xie, Q.; Feng, S.; Ullah, S.; Li, R.; Dong, J.; Li, D.; Li, Y.; Chen, X.-Q. Topological Quantum Catalyst: Dirac Nodal Line States and a Potential Electrocatalyst of Hydrogen Evolution in the TiSi Family. *Sci. China Mater.* **2018**, *61*, 23–29.

(21) Wang, A.; Shen, L.; Zhao, M.; Wang, J.; Zhou, W.; Li, W.; Feng, Y.; Liu, H. Tungsten Boride: a 2D Multiple Dirac Semimetal for the Hydrogen Evolution Reaction. *J. Mater. Chem. C* **2019**, *7*, 8868–8873.

(22) Li, G.; Fu, C.; Shi, W.; Jiao, L.; Wu, J.; Yang, Q.; Saha, R.; Kamminga, M. E.; Srivastava, A. K.; Liu, E. et al. Dirac Nodal Arc Semimetal PtSn4: An Ideal Platform for Understanding Surface Properties and Catalysis for Hydrogen Evolution. *Angew. Chem. Int. Ed.* **2019**, *58*, 13107–13112.

(23) He, Y.; Yan, D.; Wang, S.; Shi, L.; Zhang, X.; Yan, K.; Luo, H. Topological Type-II Dirac Semimetal and Superconductor $PdTe_2$ for Ethanol Electrooxidation. *Energy Technol.* **2019**, *7*, 1900663.

(24) Li, G.; Xu, Q.; Shi, W.; Fu, C.; Jiao, L.; Kamminga, M. E.; Yu, M.; Tüysüz, H.; Kumar, N.; Süß, V. et al. Surface States in Bulk Single Crystal of Topological Semimetal $Co_3Sn_2S_2$ Toward Water Oxidation. *Sci. Adv.* **2019**, *5*, eaaw9867.

(25) Tang, M.; Shen, H.; Qie, Y.; Xie, H.; Sun, Q. Edge-State-Enhanced CO_2 Electroreduction on Topological Nodal-Line Semimetal Cu_2Si Nanoribbons. *J. Phys. Chem. C* **2019**, *123*, 2837–2842.

(26) Yang, Q.; Li, G.; Manna, K.; Fan, F.; Felser, C.; Sun, Y. Topological Engineering of Pt-Group-Metal-Based Chiral Crystals toward High-Efficiency Hydrogen Evolution Catalysts. *Adv. Mater.* **2020**, *32*, 1908518.

(27) Gupta, U.; Rajamathi, C. R.; Kumar, N.; Li, G.; Sun, Y.; Shekhar, C.; Felser, C.; Rao, C. N. R. Effect of Magnetic Field on the Hydrogen Evolution Activity Using Non-Magnetic Weyl Semimetal Catalysts. *Dalton Trans.* **2020**, *49*, 3398–3402.

(28) Kong, X.-P.; Jiang, T.; Gao, J.; Shi, X.; Shao, J.; Yuan, Y.; Qiu, H.-J.; Zhao, W. Development of a Ni-Doped VAl_3 Topological Semimetal with a Significantly Enhanced HER Catalytic Performance. *J. Phys. Chem. Lett.* **2021**, *12*, 3740–3748.

(29) Boukhvalov, D. W.; Kuo, C.-N.; Nappini, S.; Marchionni, A.; D'Olimpio, G.; Filippi, J.; Mauri, S.; Torelli, P.; Lue, C. S.; Vizza, F. et al. Efficient Electrochemical Water Splitting with $PdSn_4$ Dirac Nodal Arc Semimetal. *ACS Catal.* **2021**, *11*, 7311–7318.

(30) Wang, L.; Zhang, X.; Meng, W.; Liu, Y.; Dai, X.; Liu, G. A Topological Quantum Catalyst: The Case of Two-Dimensional Traversing Nodal Line States Associated with High Catalytic Performance for the Hydrogen Evolution Reaction. *J. Mater. Chem. A* **2021**, *9*, 22453–22461.

(31) Yang, Q.; Le, C.; Li, G.; Heine, T.; Felser, C.; Sun, Y. Enhancement of Basal Plane Electrocatalytic Hydrogen Evolution Activity via Joint Utilization of Trivial and Non-Trivial Surface States. *Appl. Mater. Today* **2021**, *22*, 100921.

(32) Yang, Q.; Li, G.; Zhang, Y.; Liu, J.; Rao, J.; Heine, T.; Felser, C.; Sun, Y. Transition Metal on Topological Chiral Semimetal PdGa with Tailored Hydrogen Adsorption and Reduction. *npj Comput. Mater.* **2021**, *7*, 207.

(33) Ren, Z.; Zhang, H.; Wang, S.; Huang, B.; Dai, Y.; Wei, W. Nitric Oxide Reduction Reaction for Efficient Ammonia Synthesis on Topological Nodal-Line Semimetal Cu_2Si Monolayer. *J. Mater. Chem. A* **2022**, *10*, 8568–8577.

(34) Liu, W.; Zhang, X.; Meng, W.; Liu, Y.; Dai, X.; Liu, G. Theoretical Realization of Hybrid Weyl State and Associated High Catalytic Performance for Hydrogen Evolution in NiSi. *iScience* **2022**, *25*, 103543.

(35) Wang, L.; Yang, Y.; Wang, J.; Liu, W.; Liu, Y.; Gong, J.; Liu, G.; Wang, X.; Cheng, Z.; Zhang, X. Excellent Catalytic Performance Toward the Hydrogen Evolution Reaction in Topological Semimetals. *EcoMat* **2023**, *5*, e12316.

(36) Meng, W.; Zhang, X.; Liu, Y.; Dai, X.; Liu, G.; Gu, Y.; Kenny, E. P.; Kou, L. Multifold Fermions and Fermi Arcs Boosted Catalysis in Nanoporous Electride $12CaO{\cdot}7Al_2O_3$. *Adv. Sci.* **2023**, *10*, 2205940.

(37) Boukhvalov, D. W.; D'Olimpio, G.; Mazzola, F.; Kuo, C.-N.; Mardanya, S.; Fujii, J.; Politano, G. G.; Lue, C. S.; Agarwal, A.; Vobornik, I. et al. Unveiling the Catalytic Potential of Topological Nodal-Line Semimetal $AuSn_4$ for Hydrogen Evolution and CO_2 Reduction. *J. Phys. Chem. Lett.* **2023**, *14*, 3069–3076.

(38) Zhu, X.; Yuan, X.; Ge, M.; Tang, Y. Unveil the Potential-Dependent Electrochemical Formate Formation on Topological $PtBi_2$ Monolayer. *ACS Appl. Energy Mater.* **2023**, *6*, 8677–8683.

(39) Zhang, H.; Liu, C.-X.; Qi, X.-L.; Dai, X.; Fang, Z.; Zhang, S.-C. Topological Insulators in Bi_2Se_3, Bi_2Te_3, and Sb_2Te_3 with a Single Dirac Cone on the Surface. *Nat. Phys.* **2009**, *5*, 438–442.

(40) Xia, Y.; Qian, D.; Hsieh, D.; Wray, L.; Pal, A.; Lin, H.; Bansil, A.; Grauer, D.; Hor, Y. S.; Cava, R. J. et al. Observation of a Large-Gap Topological-Insulator Class with a Single Dirac Cone on the Surface. *Nat. Phys.* **2009**, *5*, 398–402.

(41) Zhang, T.; Cheng, P.; Chen, X.; Jia, J.-F.; Ma, X.; He, K.; Wang, L.; Zhang, H.; Dai, X.; Fang, Z. et al. Experimental Demonstration of Topological Surface States Protected by Time-Reversal Symmetry. *Phys. Rev. Lett.* **2009**, *103*, 266803.

(42) Chen, Y. L.; Analytis, J. G.; Chu, J.-H.; Liu, Z. K.; Mo, S.-K.; Qi, X. L.; Zhang, H. J.; Lu, D. H.; Dai, X.; Fang, Z. et al. Experimental Realization of a Three-Dimensional Topological Insulator, Bi_2Te_3. *Science* **2009**, *325*, 178–181.

(43) Hsieh, D.; Xia, Y.; Qian, D.; Wray, L.; Meier, F.; Dil, J. H.; Osterwalder, J.; Patthey, L.; Fedorov, A. V.; Lin, H. et al. Observation of Time-Reversal-Protected Single-Dirac-Cone Topological-Insulator States in Bi_2Te_3 and Sb_2Te_3. *Phys. Rev. Lett.* **2009**, *103*, 146401.

(44) Zhang, W.; Yu, R.; Zhang, H.-J.; Dai, X.; Fang, Z. First-Principles Studies of the Three-Dimensional Strong Topological Insulators Bi_2Te_3, Bi_2Se_3, and Sb_2Te_3. *New J. Phys.* **2010**, *12*, 065013.

(45) Yazyev, O. V.; Moore, J. E.; Louie, S. G. Spin Polarization and Transport of Surface States in the Topological Insulators Bi_2Se_3 and Bi_2Te_3 from First Principles. *Phys. Rev. Lett.* **2010**, *105*, 266806.

(46) Zhang, Y.; He, K.; Chang, C.-Z.; Song, C.-L.; Wang, L.-L.; Chen, X.; Jia, J.-F.; Fang, Z.; Dai, X.; Shan, W.-Y. et al. Crossover of the Three-Dimensional Topological Insulator Bi_2Se_3 to the Two-Dimensional Limit. *Nat. Phys.* **2010**, *6*, 584–588.

(47) Park, K.; Heremans, J. J.; Scarola, V. W.; Minic, D. Robustness of Topologically Protected Surface States in Layering of Bi_2Te_3 Thin Films. *Phys. Rev. Lett.* **2010**, *105*, 186801.

(48) Förster, T.; Krüger, P.; Rohlfing, M. *GW* Calculations for Bi_2Te_3 and Sb_2Te_3 Thin Films: Electronic and Topological Properties. *Phys. Rev. B* **2016**, *93*, 205442.

(49) Wang, X.; Bian, G.; Miller, T.; Chiang, T.-C. Fragility of Surface States and Robustness of Topological Order in Bi_2Se_3 against Oxidation. *Phys. Rev. Lett.* **2012**, *108*, 096404.

(50) Yashina, L. V.; Sánchez-Barriga, J.; Scholz, M. R.; Volykhov, A. A.; Sirotina, A. P.; Neudachina, S., Vera; Tamm, M. E.; Varykhalov, A.; Marchenko, D.; Springholz, G. et al. Negligible Surface Reactivity of Topological Insulators Bi_2Se_3 and Bi_2Te_3 towards Oxygen and Water. *ACS Nano* **2013**, *7*, 5181–5191.

(51) Ngabonziza, P.; Heimbuch, R.; de Jong, N.; Klaassen, R. A.; Stehno, M. P.; Snelder, M.; Solmaz, A.; Ramankutty, S. V.; Frantzeskakis, E.; van Heumen, E. et al. In Situ Spectroscopy of Intrinsic Bi_2Te_3 Topological Insulator Thin Films and Impact of Extrinsic Defects. *Phys. Rev. B* **2015**, *92*, 035405.

(52) Volykhov, A. A.; Sánchez-Barriga, J.; Sirotina, A. P.; Neudachina, V. S.; Frolov, A. S.; Gerber, E. A.; Kataev, E. Y.; Senkovsky, B.; Khmelevsky, N. O.; Aksenenko, A. Y. et al. Rapid Surface Oxidation of Sb_2Te_3 as Indication for a Universal Trend in the Chemical Reactivity of Tetradymite Topological Insulators. *Chem. Mater.* **2016**, *28*, 8916–8923.

(53) Yang, J.; Zheng, B.; Chen, Z.; Xu, W.; Wang, R.; Xu, H. Robust Topological States in Bi_2Se_3 against Surface Oxidation. *J. Phys. Chem. C* **2020**, *124*, 6253–6259.

(54) Wu, J. Understanding the Electric Double-Layer Structure, Capacitance, and Charging Dynamics. *Chem. Rev.* **2022**, *122*, 10821–10859.

(55) Li, P.; Jiao, Y.; Huang, J.; Chen, S. Electric Double Layer Effects in Electrocatalysis: Insights from Ab Initio Simulation and Hierarchical Continuum Modeling. *JACS Au* **2023**, *3*, 2640–2659.

(56) Shah, A. H.; Zhang, Z.; Huang, Z.; Wang, S.; Zhong, G.; Wan, C.; Alexandrova, A. N.; Huang, Y.; Duan, X. The Role of Alkali Metal Cations and Platinum-Surface Hydroxyl in the Alkaline Hydrogen Evolution Reaction. *Nat. Catal.* **2022**, *5*, 923–933.

(57) Hohenberg, P.; Kohn, W. Inhomogeneous Electron Gas. *Phys. Rev.* **1964**, *136*, B864–B871.

(58) Kohn, W.; Sham, L. J. Self-Consistent Equations Including Exchange and Correlation Effects. *Phys. Rev.* **1965**, *140*, A1133–A1138.

(59) Perdew, J. P.; Burke, K.; Ernzerhof, M. Generalized Gradient Approximation Made Simple. *Phys. Rev. Lett.* **1996**, *77*, 3865–3868.

(60) Xiao, J.; Yan, B. First-Principles Calculations for Topological Quantum Materials. *Nat. Rev. Phys.* **2021**, *3*, 283–297.

(61) Gauthier, J. A.; Ringe, S.; Dickens, C. F.; Garza, A. J.; Bell, A. T.; Head-Gordon, M.; Nørskov, J. K.; Chan, K. Challenges in Modeling Electrochemical Reaction Energetics with Polarizable Continuum Models. *ACS Catal.* **2019**, *9*, 920–931.

(62) Ringe, S.; Hörmann, N. G.; Oberhofer, H.; Reuter, K. Implicit Solvation Methods for Catalysis at Electrified Interfaces. *Chem. Rev.* **2022**, *122*, 10777–10820.

(63) Kresse, G.; Hafner, J. Ab Initio Molecular Dynamics for Liquid Metals. *Phys. Rev. B* **1993**, *47*, 558–561.

(64) Kresse, G.; Hafner, J. Ab Initio Molecular Dynamics Simulation of the Liquid-Metal–Amorphous-Semiconductor Transition in Germanium. *Phys. Rev. B* **1994**, *49*, 14251–14269.

(65) Kresse, G.; Furthmüller, J. Efficiency of Ab-Initio Total Energy Calculations for Metals and Semiconductors Using a Plane-Wave Basis Set. *Comput. Mater. Sci.* **1996**, *6*, 15–50.

(66) Kresse, G.; Furthmüller, J. Efficient Iterative Schemes for Ab Initio Total-Energy Calculations Using a Plane-Wave Basis Set. *Phys. Rev. B* **1996**, *54*, 11169–11186.

(67) Mathew, K.; Sundararaman, R.; Letchworth-Weaver, K.; Arias, T. A.; Hennig, R. G. Implicit Solvation Model for Density-Functional Study of Nanocrystal Surfaces and Reaction Pathways. *J. Chem. Phys.* **2014**, *140*, 084106.

(68) Mathew, K.; Kolluru, V. S. C.; Mula, S.; Steinmann, S. N.; Hennig, R. G. Implicit

Self-Consistent Electrolyte Model in Plane-Wave Density-Functional Theory. *J. Chem. Phys.* **2019**, *151*, 234101.

(69) Steinmann, S. N.; Sautet, P. Assessing a First-Principles Model of an Electrochemical Interface by Comparison with Experiment. *J. Phys. Chem. C* **2016**, *120*, 5619–5623.

(70) Chang, K.; Chen, J. G.; Lu, Q.; Cheng, M.-J. Grand Canonical Quantum Mechanical Study of the Effect of the Electrode Potential on N-Heterocyclic Carbene Adsorption on Au Surfaces. *J. Phys. Chem. C* **2017**, *121*, 24618–24625.

(71) Munarriz, J.; Zhang, Z.; Sautet, P.; Alexandrova, A. N. Graphite-Supported Ptn Cluster Electrocatalysts: Major Change of Active Sites as a Function of the Applied Potential. *ACS Catal.* **2022**, *12*, 14517–14526.

(72) Zhang, Z.; Wei, Z.; Sautet, P.; Alexandrova, A. N. Hydrogen-Induced Restructuring of a Cu(100) Electrode in Electroreduction Conditions. *J. Am. Chem. Soc.* **2022**, *144*, 19284–19293.

(73) Steinmann, S. N.; Michel, C.; Schwiedernoch, R.; Sautet, P. Impacts of Electrode Potentials and Solvents on the Electroreduction of CO_2: A Comparison of Theoretical Approaches. *Phys. Chem. Chem. Phys.* **2015**, *17*, 13949–13963.

(74) Henkelman, G.; Arnaldsson, A.; Jónsson, H. A Fast and Robust Algorithm for Bader Decomposition of Charge Density. *Comput. Mater. Sci.* **2006**, *36*, 354–360.

(75) Sanville, E.; Kenny, S. D.; Smith, R.; Henkelman, G. Improved Grid-Based Algorithm for Bader Charge Allocation. *J. Comput. Chem.* **2007**, *28*, 899–908.

(76) Tang, W.; Sanville, E.; Henkelman, G. A Grid-Based Bader Analysis Algorithm Without Lattice Bias. *J. Phys. Condens. Matter* **2009**, *21*, 084204.

(77) Kim, M.; Kim, C. H.; Kim, H.-S.; Ihm, J. Topological Quantum Phase Transitions

Driven by External Electric Fields in Sb_2Te_3 Thin Films. *Proc. Natl. Acad. Sci.* **2012**, *109*, 671–674.

(78) Zhang, T.; Ha, J.; Levy, N.; Kuk, Y.; Stroscio, J. Electric-Field Tuning of the Surface Band Structure of Topological Insulator Sb_2Te_3 Thin Films. *Phys. Rev. Lett.* **2013**, *111*, 056803.

(79) Wang, D.; Chen, L.; Liu, H.; Wang, X. Topological phase transitions in Sb(111) films driven by external strain and electric field. *Europhys. Lett.* **2014**, *104*, 57011.

(80) Liu, Q.; Zhang, X.; Abdalla, L. B.; Fazzio, A.; Zunger, A. Switching a Normal Insulator into a Topological Insulator via Electric Field with Application to Phosphorene. *Nano Lett.* **2015**, *15*, 1222–1228.

(81) Qi, J.; Li, X.; Qian, X. Electrically Controlled Band Gap and Topological Phase Transition in Two-Dimensional Multilayer Germanane. *Appl. Phys. Lett.* **2016**, *108*, 253107.

(82) Baba, Y.; Amado, M.; Diez, E.; Domínguez-Adame, F.; Molina, R. A. Effect of External Fields in High Chern Number Quantum Anomalous Hall Insulators. *Phys. Rev. B* **2022**, *106*, 245305.